

# Additive manufacturing of 3D yttria-stabilized zirconia microarchitectures

J.P. Winczewski<sup>a,1,\*</sup>, S. Zeiler<sup>b,c,1,\*</sup>, S. Gabel<sup>b</sup>, D. Maestre<sup>d</sup>, B. Merle<sup>b,e</sup>, J.G.E. Gardeniers<sup>a</sup>,  
A. Susarrey Arce<sup>a,\*</sup>

<sup>a</sup> Mesoscale Chemical Systems, MESA<sup>+</sup> Institute, University of Twente, P.O. Box 217, Enschede, 7500 AE, The Netherlands

<sup>b</sup> Materials Science & Engineering, Institute I, Friedrich-Alexander-Universität Erlangen-Nürnberg, Martensstr. 5, Erlangen 91058, Germany

<sup>c</sup> Department of Materials Science, Montanuniversität Leoben, Roseggerstr. 12, Leoben 8700, Austria

<sup>d</sup> Department of Materials Physics, Faculty of Physics, Complutense University of Madrid, Madrid 28040, Spain

<sup>e</sup> Institute of Materials Engineering, University of Kassel, Moenchebergstr. 3, Kassel 34125, Germany

## ARTICLE INFO

### Keywords:

Additive manufacturing  
3D printing  
Yttria-stabilized zirconia  
Photoluminescence  
Micromechanics

## ABSTRACT

The additive manufacturing (AM) of yttria-stabilized zirconia (YSZ) microarchitectures with sub-micrometer precision via two-photon lithography (TPL), utilizing custom photoresin containing zirconium and yttrium monomers is investigated. YSZ 3D microarchitectures can be formed at low temperatures (600 °C). The low-temperature phase stabilization of ZrO<sub>2</sub> doped with Y<sub>2</sub>O<sub>3</sub> demonstrates that doping ZrO<sub>2</sub> with ≈ 10 mol% Y<sub>2</sub>O<sub>3</sub> stabilizes the *c*-ZrO<sub>2</sub> phase. The approach does not utilize YSZ particles as additives. Instead, the crystallization of the YSZ phase is initiated after printing, i.e., during thermal processing in the air at 600 °C – 1200 °C for one and two hours. The YSZ microarchitectures are characterized in detail. This includes understanding the role of defect chemistry, which has been overlooked in TPL-enabled micro-ceramics. Upon UV excitation, defect-related yellowish-green emission is observed from YSZ microarchitectures associated with intrinsic and extrinsic centers, correlated with the charge compensation due to Y<sup>3+</sup> doping. The mechanical properties of the microarchitectures are assessed with manufactured micropillars. Micropillar compression yields the intrinsic mechanical strength of YSZ. The highest strength is observed for micropillars annealed at 600 °C, and this characteristic decreased with an increase in the annealing temperature. The deformation behavior gradually changes from ductile to brittle-like, correlating with the Hall–Petch strengthening mechanism.

## 1. Introduction

Zirconia (ZrO<sub>2</sub>) is a high-performance ceramic material valued for chemical and mechanical resistance, applied in a diverse range of products.[1,2] Under atmospheric pressure, ZrO<sub>2</sub> is thermodynamically stable in monoclinic (*m*-ZrO<sub>2</sub>, <1170 °C), tetragonal (*t*-ZrO<sub>2</sub>, 1170–2370 °C), and cubic (*c*-ZrO<sub>2</sub>, >2370 °C) phases.[1] The *t*-ZrO<sub>2</sub> and *c*-ZrO<sub>2</sub> are typically preferred over the lower symmetry *m*-ZrO<sub>2</sub> phase for applications at room temperature.[3] These two *t*-ZrO<sub>2</sub> and *c*-ZrO<sub>2</sub> symmetric phases can be achieved at low temperatures by substituting the host cations with aliovalent dopants, such as alkaline earth or rare earth metals, i.e., lanthanides, Ca<sup>2+</sup>, Mg<sup>2+</sup>, and Y<sup>3+</sup>. [4] In the case of Y<sub>2</sub>O<sub>3</sub>, zirconia is partially stabilized at approximately 2 – 5 mol % additive concentration, yielding the metastable tetragonal (*t*\*-ZrO<sub>2</sub>) phase. [5] To achieve full stabilization, at least 8 mol % of Y<sub>2</sub>O<sub>3</sub> is necessary,

which results in metastable cubic zirconia (*c*\*-ZrO<sub>2</sub>). [5] As a result of the doping, oxygen vacancies (V<sub>O</sub>) are introduced in the metastable analogs to maintain a neutral charge. [3] Charge neutrality is associated with two Y<sup>3+</sup> ions compensating for one oxygen vacancy. [3] Due to the co-existence of the V<sub>O</sub> and dopant ions, the local atomic environments in the *t*\*-ZrO<sub>2</sub> and *c*\*-ZrO<sub>2</sub> are significantly different from the pure stoichiometric phases. [5]

The stabilization of ZrO<sub>2</sub> significantly alters its properties. The melting point of YSZ exceeding that of most metal oxides, combined with low thermal conductivity, makes it a material of choice for thermal barrier coatings and refractories. [6,7] The high ionic conductivity and electronic resistivity render YSZ the most-applied solid oxide fuel cell electrolyte. [8] Furthermore, the biocompatibility, mechanical stability, fracture resistance, and aesthetic appearance of YSZ are advantageous in dentistry, e.g., tooth crowns, inlays, or implant abutments. [1,9] These

\* Corresponding authors at: Mesoscale Chemical Systems, MESA<sup>+</sup> Institute, University of Twente, P.O. Box 217, Enschede, 7500 AE, The Netherlands (J.P. Winczewski, A. Susarrey-Arce); and Department of Materials Science, Montanuniversität Leoben, Roseggerstr. 12, 8700 Leoben, Austria (S. Zeiler).

E-mail addresses: [j.p.winczewski@gmail.com](mailto:j.p.winczewski@gmail.com) (J.P. Winczewski), [stefan.zeiler@unileoben.ac.at](mailto:stefan.zeiler@unileoben.ac.at) (S. Zeiler), [a.susarreyarce@utwente.nl](mailto:a.susarreyarce@utwente.nl) (A. Susarrey Arce).

<sup>1</sup> These authors contributed equally to this work.

<https://doi.org/10.1016/j.matdes.2024.112701>

Received 16 September 2023; Received in revised form 20 December 2023; Accepted 23 January 2024

Available online 1 February 2024

0264-1275/© 2024 The Author(s). Published by Elsevier Ltd. This is an open access article under the CC BY license (<http://creativecommons.org/licenses/by/4.0/>).

properties and extensive advanced applications stimulated the demand for YSZ, benefiting dimensional refinement.

In recent years, methods of producing structured YSZ have emerged, including electrospinning of nanofibers,[10,11] preparation of hollow tubes through the combination of phase inversion with sintering,[12] or microtubes via direct fiber drawing with self-arrangement.[13] More effective methods granting the desired three-dimensional (3D) design involve direct laser beam sintering,[14] extrusion printing,[15] stereolithography,[16] or digital light processing (DLP).[17,18] The common ground of the abovementioned methods is the formulations, typically established by the dispersion of YSZ particles. YSZ particles impose a penalty to feature size resolution during TPL. Recently, Desponds *et al.* presented surface functionalization of commercially available 5 nm yttrium (8 mol%) stabilized ZrO<sub>2</sub> nanoparticles (NPs) with 2-carboxyethyl acrylate.[19] The YSZ NPs were then supplemented to the mixture containing zirconium bromonorborelactone carboxylate triacrylate, dipentaerythritol penta-/hexa-acrylate, 2-butanone, and Michler's ketone, and later used as a photoresin in TPL to fabricate 3D microarchitectures.[19] After the thermal treatment for the removal of organic matter, solid shrunken replicas were obtained.[19] However, introducing NPs is challenging as realizing advanced 3D structures would require the technical possibility of manufacturing monodisperse NPs with the desired chemical composition. If NP polydispersity is achieved, the NPs should be small enough to reduce scattering without compromising sub-micrometer printing precision. Additionally, NP loading should remain as low as possible, not compromising printing resolution. At the same time, loading should be high enough to retain the shape of the pre-ceramic replica after the temperature treatment required to remove organics while maintaining sintering low.

A way forward is a one-pot preparation of photoresin containing monomeric salts. The approach is less laborious, and the key advantage of this method is the possibility of directly tuning the chemical composition by simply modifying the content of the salts or doping. In this work, we utilize Zr and Y monomers, permitting the sculpting of pre-ceramic microarchitectures *via* TPL. The additively-manufactured structures are annealed in the air, and the organic matrix is burned off. Solid ceramic replicas of linearly decreased feature sizes are formed. Introducing  $\approx 10$  mol % Y<sub>2</sub>O<sub>3</sub> ( $\approx 17.0$  wt% Y<sub>2</sub>O<sub>3</sub>) promotes stabilization of ZrO<sub>2</sub> in cubic phase at temperatures as low as 600 °C, while higher treatment temperatures increase the crystallinity. The distribution of Y and Zr is studied throughout the 3D microarchitecture fabrication

process. The morphology, chemical composition, and optical properties of the synthesized 3D microarchitectures are evaluated through photoluminescence measurements. The mechanical properties resulting from the additive manufacturing process are investigated by micropillar compression on plain specimens, which permits the assessment of the intrinsic mechanical strength of YSZ fabricated using TPL.

## 2. Results

### 2.1. The additive manufacturing of yttria-stabilized zirconia microarchitectures

The AM of YSZ microstructures requires the formulation of tailor-made photoresin (Fig. 1(a)). Metal-organic salts, zirconium acrylate, and yttrium methacrylate are dissolved in dimethylacetamide and dichloromethane mixed with acrylic acid, of Y to Zr ratio adjusted to yield approximately 10 mol % Y<sub>2</sub>O<sub>3</sub> ( $\approx 17.0$  wt% Y<sub>2</sub>O<sub>3</sub>) to ensure the formation of YSZ of the *c*-ZrO<sub>2</sub> phase. A crosslinking agent, pentaerythritol triacrylate, is added with the photoinitiator, 7-diethylamino-3-thenoylcoumarin. The excess dichloromethane is evaporated under reduced pressure. The photoresin is then applied to the chamber created by sellotaping a cover glass slide to a silicon dice with double-sided polyimide adhesive tape. TPL is used to sculpt the structures on the surface of the silicon substrate (Fig. 1(b)). The non-cured photoresin is washed off, and the 3D crosslinked pre-ceramic microstructures are annealed in the air to combust the organic constituents (Fig. 1(c)). After the thermal treatment, self-miniaturized ceramic microstructures are manufactured. The thermogravimetric analysis (TGA) assesses the thermal behavior and stability of the UV-cured photoresin (Fig. S1, Section S1, Supporting Information). Most organic matter is combusted below 500 °C, and a residue, likely the oxidation product of metal-organic precursors, is formed.

### 2.2. Morphology and structural characteristics of YSZ 3D microarchitectures

The non-annealed 3D octet-truss lattice after printing and development has an average  $33.82 \pm 0.23$   $\mu\text{m}$  edge length and a  $1.77 \pm 0.13$   $\mu\text{m}$  beam width, as observed from Scanning Electron Microscopy (SEM) images (Fig. 2(a)). Scanning Transmission Electron Microscopy (STEM) reveals no metallic or metal oxide grains formed during the

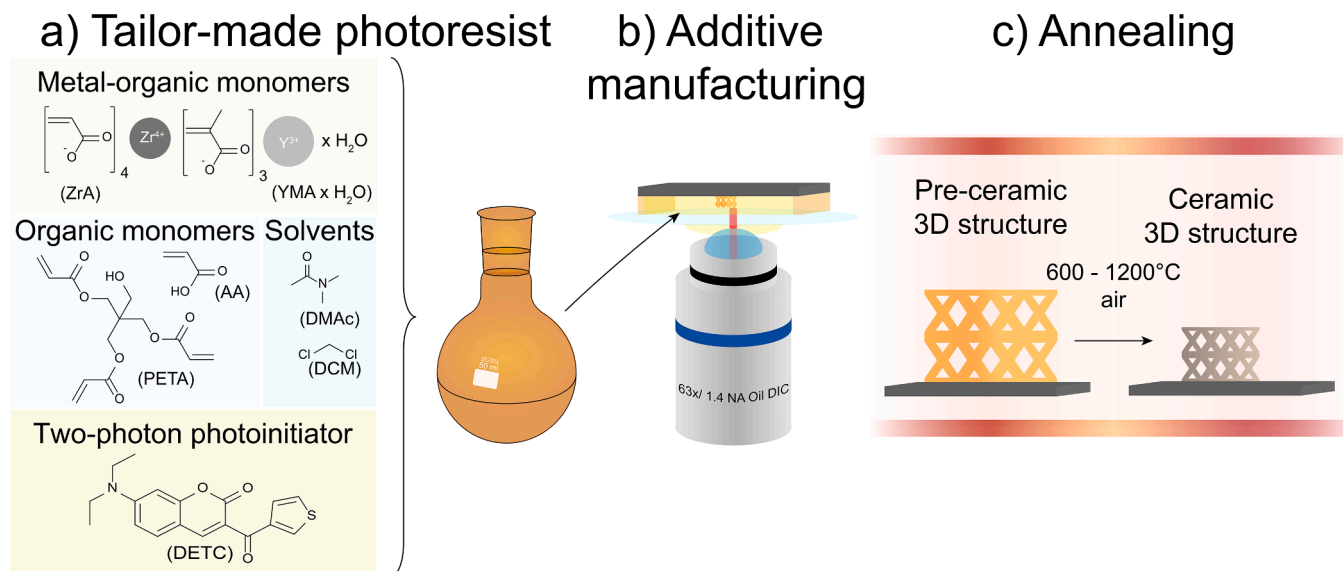


**Fig. 1.** Additive manufacturing of YSZ 3D microarchitectures: (a) preparation of the tailor-made photoresin, (b) writing the pre-ceramic 3D structures using TPL, (c) thermal annealing of the 3D-printed structures.

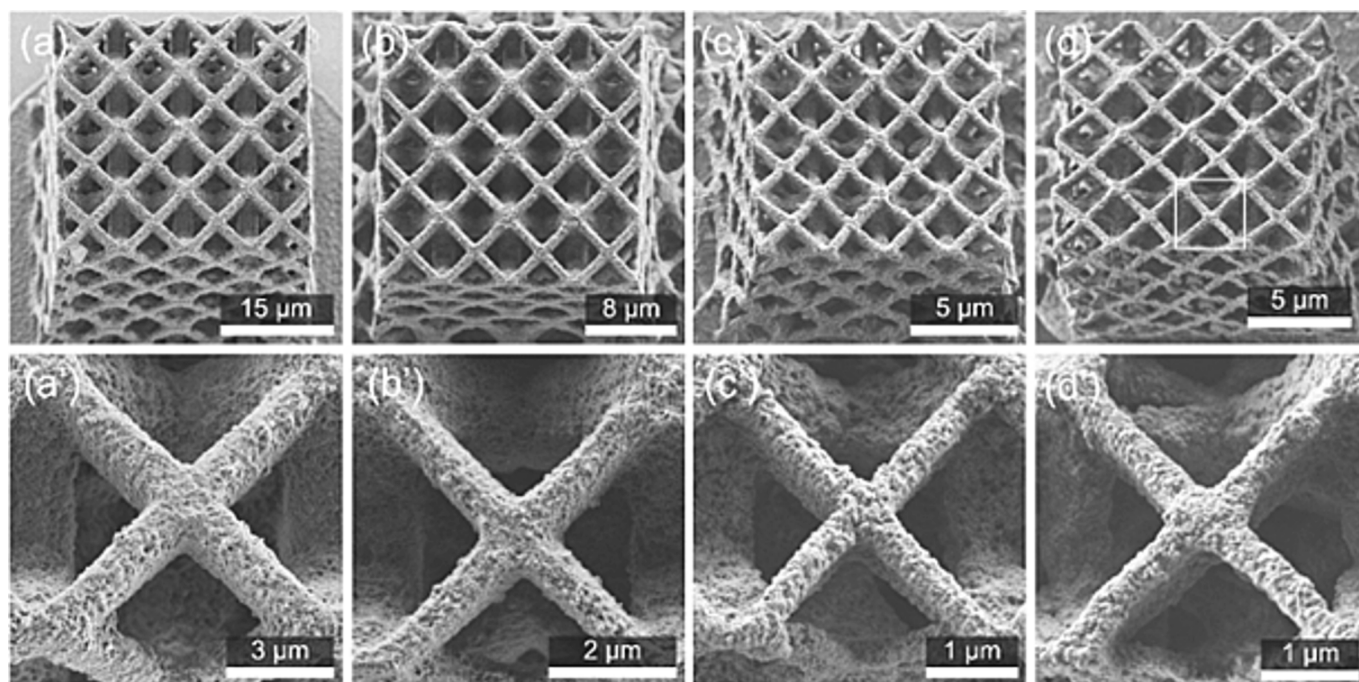


Fig. 2. Secondary electron micrographs of an octet-truss lattice (a/a') pre-ceramic state, before annealing, (b/b') heat treated to 350 °C, (c/c') annealed at 600 °C for 1 h, (d/d') annealed at 1200 °C for 2 h.

photopolymerization of zirconium acrylate and yttrium methacrylate hydrate, signifying the precursor compatibility, miscibility, and likely formation of a copolymer (Fig. S2, Section S2, Supporting Information).

The slow heating ramp of  $0.5\text{ }^{\circ}\text{C min}^{-1}$  to 350 °C, then  $1\text{ }^{\circ}\text{C min}^{-1}$  to the target temperature, preserves the 3D object integrity and promotes the organic constituent decomposition. A representative micrograph of the sample heated to 350 °C is given in Fig. 2(b). The reduction of edge length and beam width to  $18.85 \pm 0.13\text{ }\mu\text{m}$  ( $\approx 44\%$ ) and  $0.79 \pm 0.05\text{ }\mu\text{m}$  ( $\approx 55\%$ ) is associated with the thermal decomposition of the organic matrix (Table S1, Supporting Information). The annealing at 600 °C for 1 h results in the further reduction of the features to approximately  $14.42 \pm 0.22\text{ }\mu\text{m}$  ( $\approx 57\%$ ) and  $0.58 \pm 0.06\text{ }\mu\text{m}$  ( $\approx 67\%$ ), as shown in Fig. 2(c). The edge length and beam width in the sample annealed at 1200 °C for 2 h reach  $11.85 \pm 0.15\text{ }\mu\text{m}$  ( $\approx 65\%$ ) and  $0.43 \pm 0.04\text{ }\mu\text{m}$

( $\approx 76\%$ ); the surface appears polycrystalline and irregular grains with sharp edges are observed in Fig. 2(d). The low-magnification bright-field STEM image (Fig. 3(a)) of a lamella extracted from the octet-truss lattice annealed at 1200 °C for 2 h unveils that the structure is made of grains with an average  $121 \pm 21\text{ nm}$  length and  $89 \pm 15\text{ nm}$  width (Fig. S3, Supporting Information). The high-angle annular dark field (HAADF) micrograph unveils the crystalline lattice (Fig. 3(b)); the Fast Fourier Transform (FFT) pattern corresponding to the labeled area is presented, with the marked (1 1 1) diffraction. The line profile indicates the 0.30 nm d-spacing, corresponding to the (1 1 1) diffraction of the cubic YSZ system (Fig. S3, Supporting Information).

Images of octet-truss lattices annealed at 600 °C, 750 °C, 900 °C, 1050 °C, and 1200 °C for one and two hours are given (Figs. S4 and S5, Supporting Information). Microarchitectures treated below 1050 °C are

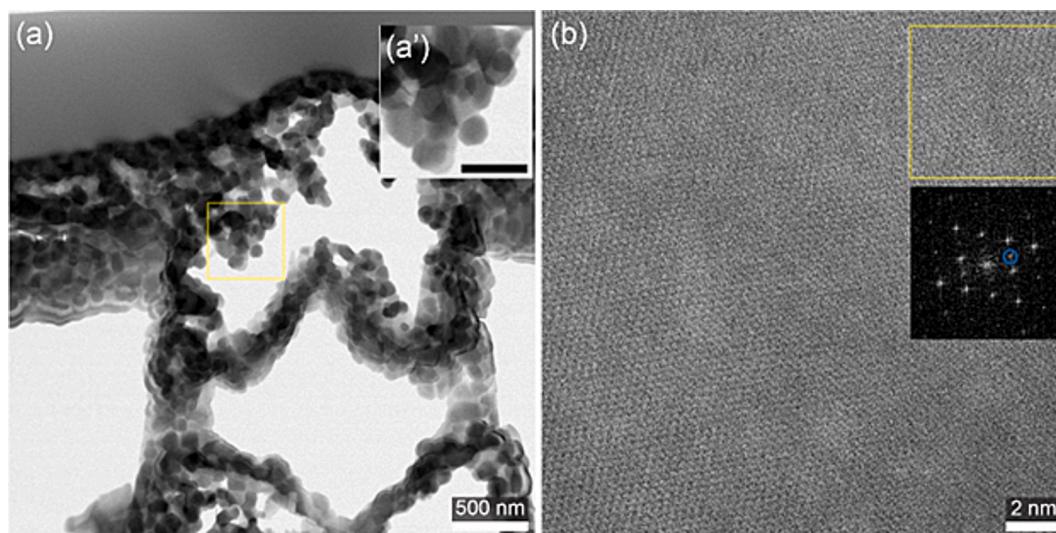


Fig. 3. (a) STEM BF micrograph of a lamella of 10 mol% YSZ annealed at 1200 °C for 2 h, presenting grains and (a') an inset with higher magnification of the labeled region and a scale bar representing 200 nm, (b) HAADF image with the labeled area corresponding to the Fast Fourier Transform (FFT) pattern with (1 1 1) spot marked, indicating the 0.30 nm d-spacing (inset).



made of crystallites that cannot be individually resolved even at high SEM magnification. The microstructure dimensions remain stable ( $\approx 12\text{--}14\ \mu\text{m}$  and  $\approx 0.4\text{--}0.6\ \mu\text{m}$  edge length and beam width, respectively) after thermal treatments at  $600\ \text{°C}$  –  $1200\ \text{°C}$  (Table S1, Supporting Information).

Insights into the crystallinity of synthesized materials are provided through XRD measurements. Control 10 mol% YSZ powders are synthesized from the photoresins cured in bulk with ultraviolet light and annealed at  $600\ \text{°C}$ ,  $750\ \text{°C}$ ,  $900\ \text{°C}$ ,  $1050\ \text{°C}$  and  $1200\ \text{°C}$  for one and two hours (Fig. S6, Supporting Information). The findings point toward the formation of  $c^*\text{-ZrO}_2$  and are comparable with YSZ obtained from the annealed carbon-rich precursor mixtures (Section S4, Supporting Information).[20,21] No distinct peaks for  $\text{Y}_2\text{O}_3$  or  $t^*\text{-ZrO}_2$ , or  $m\text{-ZrO}_2$  are detected (Figs. S7 and S8, Supporting Information).[22] The average crystallite sizes (Table S2, Supporting Information) are computed using the Scherrer formula (Fig. S8 and Section S5, Supporting Information). The d-spacing ( $0.30\ \text{nm}$ ) corresponding to the most intense peak (111) agrees with the value determined with STEM. A significant crystallite size increase is noticed when the annealing temperature exceeds  $900\ \text{°C}$ ; no substantial changes occur upon extension of time from one to two hours. Similar observations can be drawn from the SEM image analysis, as the grains remain below the resolution threshold for temperatures below  $1050\ \text{°C}$  (Figs. S4 and S5, Supporting Information).

### 2.3. The chemical composition of YSZ 3D microarchitectures

Scanning Electron Microscopy – Energy Dispersive X-ray spectroscopy (SEM-EDX) is applied to assess the spatial element allocation throughout the octet-truss lattice annealed at  $1050\ \text{°C}$  for 2 h. The Zr, Y, and O distributions show that no areas are deficient with Zr or Y within the spatial resolution. SEM well aligns with XRD results for 10 % mol YSZ in Figs. S7 and S8, where only the YSZ phase has been found. The surface of the Si substrate is oxidized with native oxide. The collected

EDX spectrum (Fig. 4(b)) confirms that the Zr to Y ratio is  $\approx 3.7:1$ , thus slightly higher than expected from the 10 mol %  $\text{Y}_2\text{O}_3$  doping in  $\text{ZrO}_2$ . Peaks confirming the presence of Zr, Y, and O within the octet-truss lattice are found.[23] The main Si  $\text{K}\alpha_1$  peak, overlapping with weaker  $\text{K}\alpha_2$  and  $\text{K}\beta_1$  signals, originates from the substrate, whose surface is oxidized, thus, also associated with the O  $\text{K}\alpha_1$ . In the inset, a narrower  $1.82\text{--}2.5\ \text{keV}$  range is given, in which the characteristic Y  $\text{L}\alpha_1$ , Y  $\text{L}\alpha_2$ , Y  $\text{L}\beta_1$ , Zr  $\text{L}\alpha_1$ , Zr  $\text{L}\alpha_2$ , Zr  $\text{L}\beta_1$ , and Zr  $\text{L}\beta_2$  contributions are labeled.[23]

Owing to the high sensitivity towards oxygen ion polarizability, Raman spectroscopy is a powerful instrument to determine the symmetry of stabilized zirconia.[24,25] The Raman spectrum of fully stabilized zirconia is typically dominated by broadband within the  $530\text{--}670\ \text{cm}^{-1}$  range and several weaker poor definition features linked with the disordered oxygen sub-lattice.[25,26] In the  $\text{ZrO}_2$  stabilized with varied  $\text{Y}_2\text{O}_3$  contents, the  $645\ \text{cm}^{-1}$  band correlates with the Zr-O bond stretching and shifts to lower wavenumbers with the increase of the  $\text{Y}_2\text{O}_3$ . [27] The precise fitting of the broad, asymmetric band of  $c\text{-ZrO}_2$  at  $600\text{--}625\ \text{cm}^{-1}$  ( $\text{F}_{2g}$ ) is nontrivial; thus, in practice, the local intensity maximum value is used instead as a reference.[27,28] The thermal annealing effect on the crystallographic phase of the 3D YSZ microarchitectures at  $600\ \text{°C}$ ,  $750\ \text{°C}$ ,  $900\ \text{°C}$ ,  $1050\ \text{°C}$ , and  $1200\ \text{°C}$  for one and two hours are studied with Raman within  $50\text{--}850\ \text{cm}^{-1}$  range (Fig. 5).

The Raman spectra collected for all the 3D microarchitectures have similar shapes and profiles of the 8–10 mol% YSZ (Fig. 5) [29,30] and resemble  $\text{ZrO}_2$  stabilized with  $\geq 17\ \text{wt}\%$   $\text{Y}_2\text{O}_3$ , as the  $\text{F}_{2g}$  peak is centered at approximately  $612\ \text{cm}^{-1}$ . [27] The prominent  $t\text{-ZrO}_2$  peak at  $641\ \text{cm}^{-1}$  is not observed for any microarchitectures. Raman analysis confirms the yttria-stabilized  $c^*\text{-ZrO}_2$  phase for the 3D microarchitectures manufactured in this study under different thermal conditions, which agrees with the TEM, XRD, and SEM-EDX results discussed in the previous section. A Si/ $\text{SiO}_2$  substrate transverse optic peak ( $\approx 521\ \text{cm}^{-1}$ ), noted with an asterisk (\*), is sometimes detected. [31] Carbon-borne residues are often

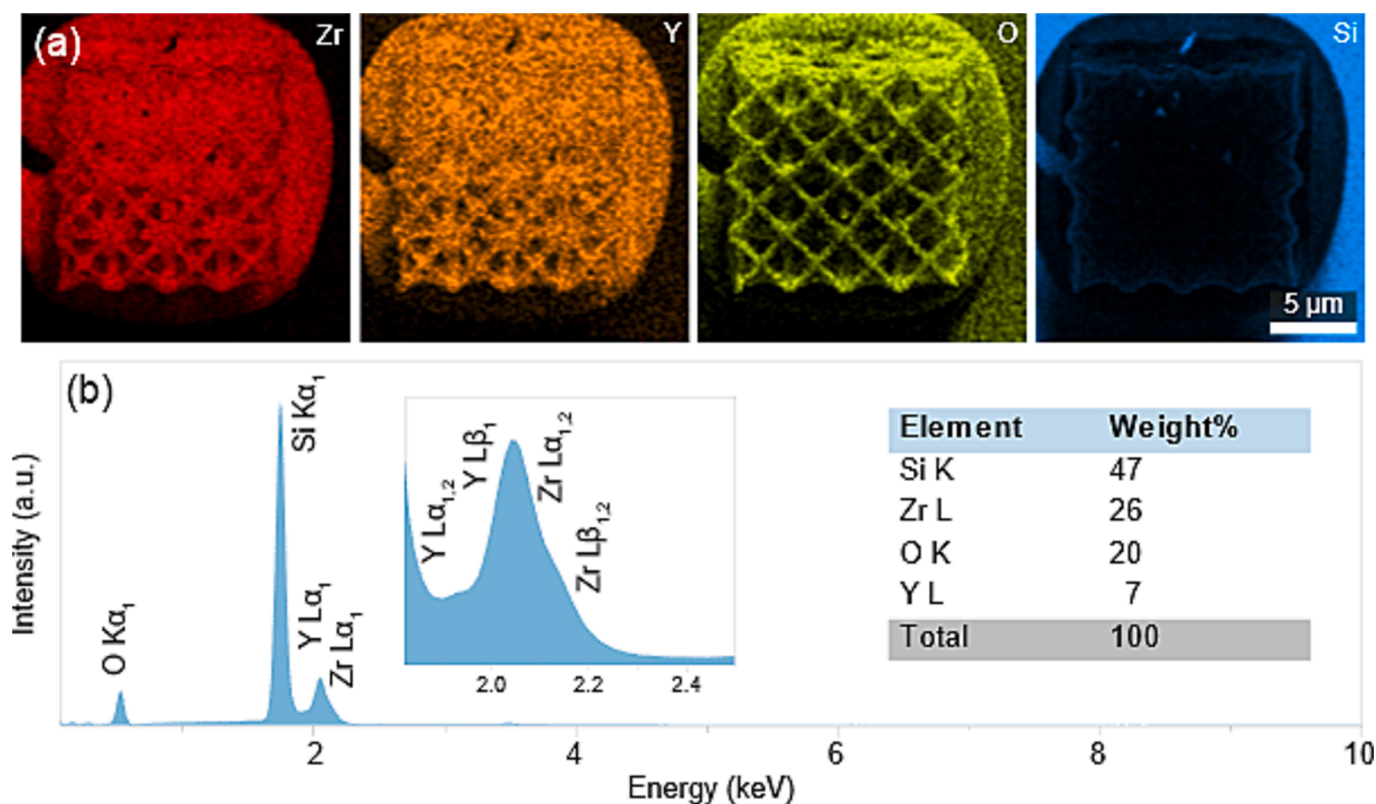
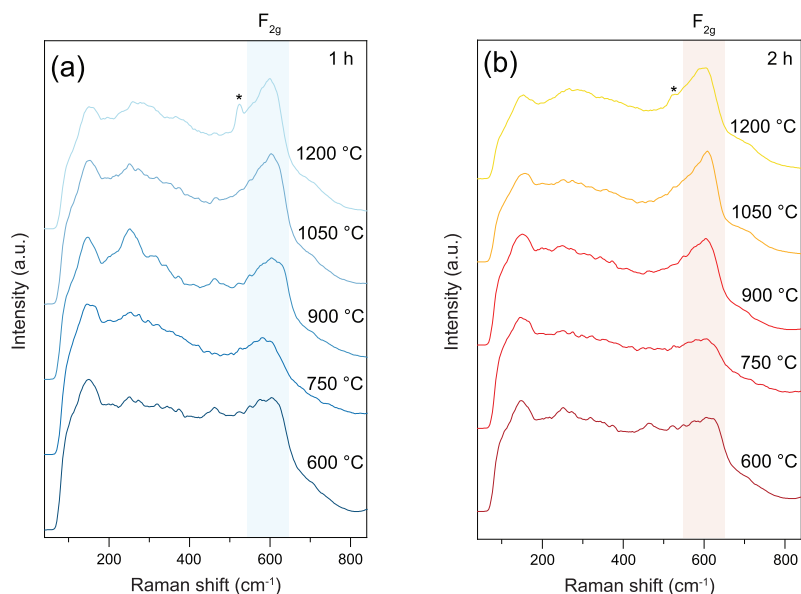


Fig. 4. (a) SEM-EDX images showing the distribution of Zr, Y, O, and Si throughout the octet-truss lattice printed on a Si substrate annealed at  $1050\ \text{°C}$  for 2 h, and (b) corresponding EDX spectrum.



**Fig. 5.** Raman spectra of 3D structures annealed at 600 °C, 750 °C, 900 °C, 1050 °C, and 1200 °C for (a) one hour and (b) two hours. The  $F_{2g}$  mode region is labeled. A substrate peak (Si) is detected in some cases, noted with an asterisk (\*).

incorporated in ceramic materials synthesized from metal-organic precursors and polymeric mixtures.[32] However, no intense vibrational modes typical for the disordered (*D*) or graphitic (*G*) carbon species are detected in a typical analytical range (Fig. S9, Supporting Information). [33,34]

Determining chemical composition at the surface of the YSZ 3D microarchitectures with XPS is complicated due to the low amount of

analyte within the spot size. Therefore, YSZ powders have been analyzed with XPS to generate complementary information about surface elemental composition, stoichiometry, and chemical state.[23] Although XPS is a surface-sensitive technique, the molar ratio of  $Y_2O_x$  to  $ZrO_{1-x}$  is approximately 0.093 – 0.095:1 for all the samples, marginally lower than the expected 0.1:1. Furthermore, the general survey confirms that Zr, O, Y, and C, and trace amounts of Hf are present in the reference

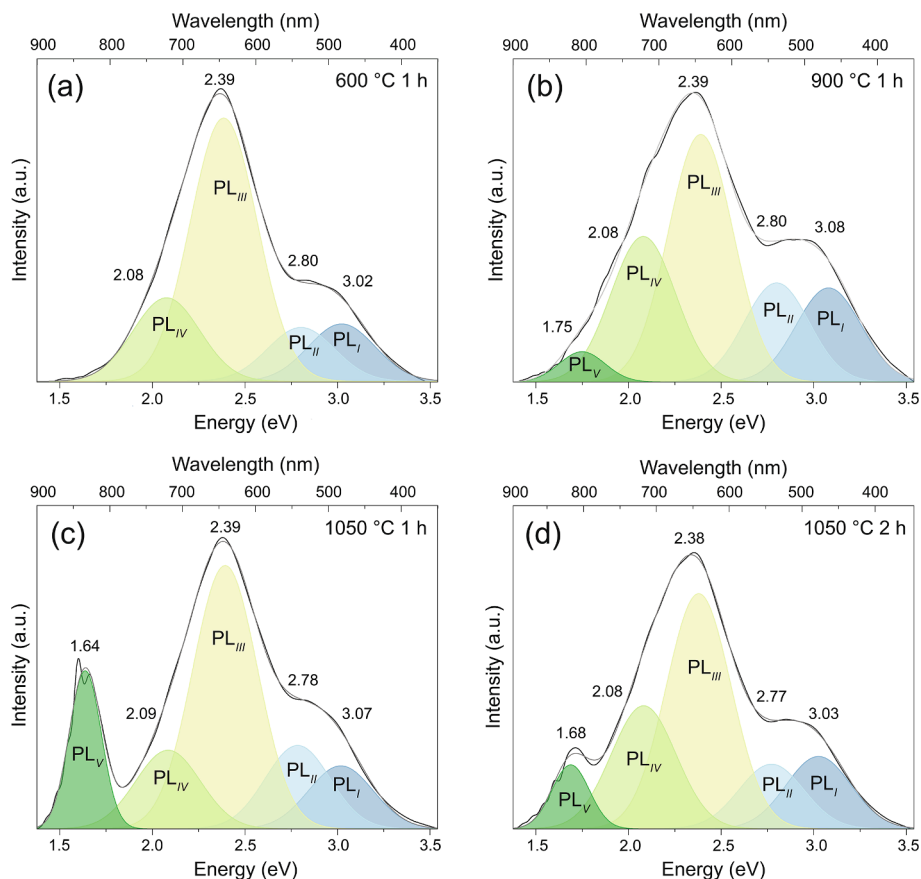


**Fig. 6.** Deconvoluted  $\mu$ -PL emission spectra of 10 mol% YSZ octet-truss lattices annealed for 1 h at (a) 600 °C, (b) 900 °C (c) 1050 °C, and for 2 h at (d) 1050 °C.

powders annealed at 600 °C, 900 °C, 1050 °C for 1 h, and at 1050 °C for 2 h (Fig. S10 Supporting Information). Hf (1 – 3 wt%) is a common impurity in Zr-based compounds, [1,35,36] while rare earth elements (i. e., Yb) have comparable atomic radii and similar cationic charges to Y, rendering them difficult to separate. [32,33]

The Zr 3d, Y 3d, O 1 s, and C 1 s core level spectra are deconvoluted (Figs. S11 and S12, Supporting Information), confirming the formation of a mixed Zr and Y oxide, with a portion of a reduced stoichiometry side-product. The amount of non-stoichiometric product reduces with the increase in annealing temperature. The C-based impurities are likely adsorbates from the combustion of the organic constituents of the prepolymeric photoresin. However, no characteristic Zr- or Y- carbonates or oxycarbonates are detected.

#### 2.4. Understanding the role of $Y^{3+}$ sites in YSZ 3D microarchitectures optically

The additive manufacturing community somehow overlooks the understanding of defects in 3D microarchitectures. However, defects can be important in multiple applications, such as solid electrolytes or micro-optoelectronics. [37,38] Therefore, the optical properties of chosen YSZ architectures are characterized using micro-photoluminescence ( $\mu$ -PL) emission measurements under 325 nm excitation. The emission spectra of the YSZ octet-truss lattices annealed at 600 °C for 1 h, 900 °C for 1 h, 1050 °C for 1 h, and 1050 °C for 2 h are recorded (Fig. 6). After the deconvolution, the  $\mu$ -PL emission spectra from the microarchitecture treated at 600 °C for 1 h comprise four peaks, labeled  $PL_I - PL_{IV}$  for simplicity. The spectra registered for the other three microarchitectures are fitted using five synthetic Gaussian curves, with an additional  $PL_V$  component at  $\approx 1.75 - 1.64$  eV. All spectra are dominated by the  $PL_{III}$  emission, and the  $PL_I - PL_{IV}$  peaks are marginally shifted between the microarchitectures. The integrated areas of  $PL_I$  and  $PL_{II}$  are similar, while the  $PL_{IV}$  is approximately 1.5 – 2 times higher. The major difference between the microarchitectures concerns the presence of the  $PL_V$  peak and its relative intensity, which is the highest in the microarchitecture annealed at 1050 °C for 1 h. The origin of the assigned contributions is discussed below.

In YSZ, for two substitutional  $Y^{3+}$  sites, one anion vacancy is introduced. [39] Since the full stabilization of the cubic phase mandates high dopant ion ( $Y^{3+}$ ) concentrations, a highly defective structure is required for charge compensation within the anionic and cationic sublattice. [40] The most prevalent defect is anionic vacancies, also responsible for the characteristic YSZ emissions. [40] Intrinsic and extrinsic type defects in YSZ are distinguished, with the vacancy neighbored exclusively by the  $Zr^{4+}$  ions or, in the latter case, by one or two  $Y^{3+}$  ions. [40] Considering the singly-occupied  $V_O$  of an oxide, its ground state can reside below the valence band ( $V_B$ ). [40] An additional electron can be introduced upon excitation, resulting in the  $V_B$  hole formation and the rise of intrinsic (F) or extrinsic ( $F_A$  and  $F_{AA}$ ) centers. [40] Petrik *et al.* associated the F,  $F_A$ , and  $F_{AA}$  centers with singly-occupied anion vacancies, corresponding to the  $PL_{II}$  ( $\approx 2.69 \pm 0.02$  eV),  $PL_{III}$  ( $\approx 2.25 \pm 0.04$  eV), and  $PL_{IV}$  ( $\approx 2.07 \pm 0.05$  eV) emissions, respectively. [40] The  $PL_I$  component was previously associated with the ionized  $V_O$  ( $F^+$ ) centers in the  $ZrO_2$  conduction band. [41,42] Upon photon absorption, a generated hole and electron allocated at  $V_O$  recombine, resulting in the  $PL_I$  emission. [41] The emissions around 2.6 eV have been previously correlated with carbon impurities in  $ZrO_2$ , though we do not observe the direct correlation of the  $\mu$ -PL emission and C 1 s or O 1 s components within XPS spectra; thus, we exclude this assignment. [43]

The assignment of the  $PL_V$  origin is complex and ambiguous. Berlin *et al.* correlated the 1.62 eV emission in  $ZrO_2$  with the Zr-O bond distortion or strain, serving the recombination center role. [41] We cannot exclude the presence of impurities in YSZ 3D Microarchitectures, e.g., Hf. Boffelli *et al.* associated the band at 1.76 eV with the luminescence from the  $V_O$  in  $HfO_2$ . [44] The cathodoluminescence peak at 1.65 eV was also assigned to  $Hf^{4+}$  or other transition element traces. [45] The

contamination of zirconium compounds with Hf is commonly reported since the  $Zr^{4+}$  and  $Hf^{4+}$  ionic radii are similar, and high-cost purification is only practiced when topmost purity is required (e.g., nuclear reactors). [1,35] The YSZ 3D microstructures and the annealing processes required in manufacturing are complex physical and chemical environments. Partial reduction of the impurities, previously observed in  $ZrO_2$  3D microarchitectures doped with lanthanide species, cannot be excluded. [46,47] The assignment  $PL_V$  signal origin remains partly ambiguous and open. The luminescence emission spectra of zirconia are often reported in the narrow range above 1.77 eV (700 nm), and the red region is typically not covered nor discussed. [48,49] Regardless, the  $\mu$ -PL emission spectra and their identified components for 10 mol% YSZ octet-truss lattices annealed agree with the literature and are maintained stable through the annealing conditions applied in this study. [40,41,50]

#### 2.5. Understanding the intrinsic mechanical properties of YSZ microarchitectures

The mechanical properties of the 3D-printed 10 mol% YSZ microarchitectures are evaluated through *in-situ* microcompression tests. A plain micropillar geometry is used to assess the intrinsic properties of the TPL-produced materials. In this study, 10 mol% YSZ micropillars annealed at 600 °C, 900 °C, and 1050 °C for 1 h and 1050 °C for 2 h are investigated. Corresponding SEM micrographs are provided in Fig. S13 (Supporting Information).

Micropillars are compressed with a flat punch indenter in a displacement-controlled mode at 20 nm/s. The experiment is halted upon fracture of the specimens, and no further deformation is applied (Fig. 7). Only well-aligned pillars are considered for the tests. The experimental data are back-extrapolated towards the origin to compensate for the initially non-ideal punch-micropillar contact, and the strain values are correspondingly shifted. This data treatment permits identifying and fitting the initial linear stress vs. strain curve segment. An SEM video of the micropillar compression is presented (Video 1, Supporting Information).

The micropillars annealed for 1 h at 600 °C, 900 °C, and 1050 °C failed at  $2.33 \pm 0.28$  GPa,  $2.23 \pm 0.62$  GPa, and  $1.43 \pm 0.18$  GPa, respectively. On average, increasing the annealing temperature decreases the ductility and strength and increases the stiffness. In the case of the 2 h heat treatment at 1050 °C, brittle-like failure occurs at  $1.98 \pm 0.30$  GPa. Our previous study investigated the mechanical properties of pure zirconia microarchitectures produced *via* TPL, which were heat-treated at different temperatures. [51] The YSZ of the micropillars annealed at 600 °C for 1 h yielded similar results to the *m*- $ZrO_2$  annealed at 1200 °C for 1 h ( $2.43 \pm 0.19$  GPa), while the pillars annealed at 1050 °C for 1 h can be compared with the *t*- $ZrO_2$  previously reported micropillars annealed at 840 °C for 1 h ( $1.29 \pm 0.33$  GPa). [51]

The micropillar cross-sections before the deformation are exposed *via* focused ion beam (FIB) milling (Fig. 8) to provide further insight into their internal morphology. In the case of 1 h thermal treatment at 600 °C, no individual grains or voids discernible at the image resolution is observed. A considerable nanopore density is found in a micropillar treated for 1 h at 900 °C. The gradual nanopore size augmentation at the expense of their population is noted after annealing at 1050 °C for 1 and 2 h. In the micropillar annealed at 1050 °C for 1 h, pores accumulate in the upper half central area, while the 2 h thermal treatment yields a more even pore distribution.

We previously compressed  $ZrO_2$  micropillars and observed “*brick and mortar*” interaction between crystallites and carbon remnants from incomplete pre-ceramic metal-organic photopolymer combustion at 600 °C, leading to increased compression strength and ductility. [51] The different annealing conditions in this study eliminate the carbon-based residues, as confirmed by Raman spectroscopy (Fig. S9, Supporting Information). Also, no point defect carbon-related emissions, dependent on the annealing temperature, are observed in the  $\mu$ -PL spectra (Fig. 6). [46] Therefore, the mechanical properties of 10 mol%

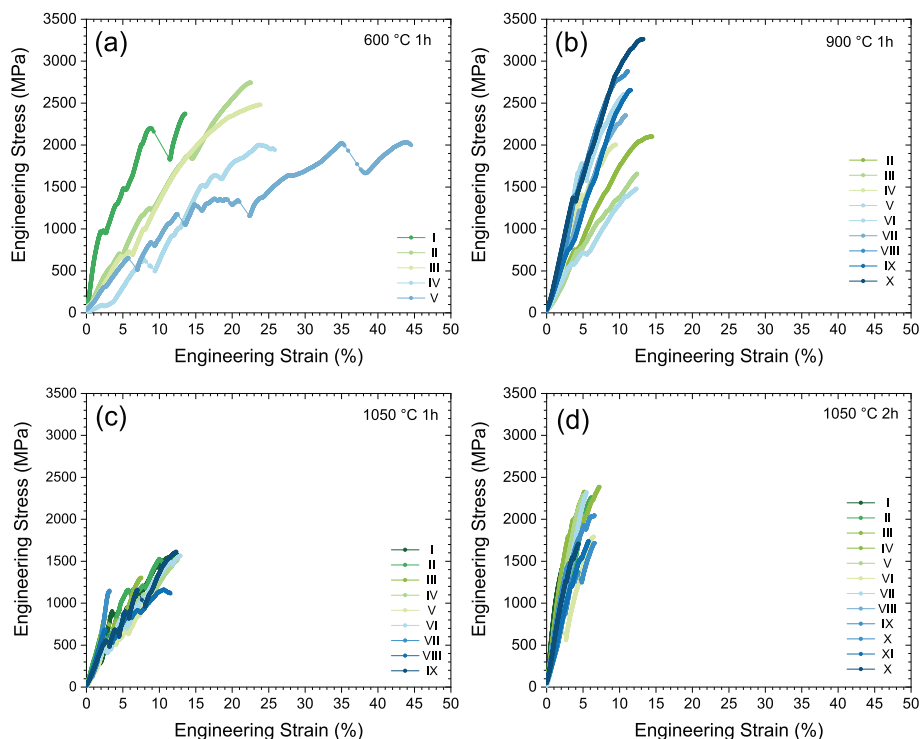


**Fig. 7.** Engineering stress vs. engineering strain curves for 10 mol % YSZ micropillars annealed for 1 h at (a) 600 °C, (b) 900 °C, (c) 1050 °C, and (d) for 2 h at 1050 °C.

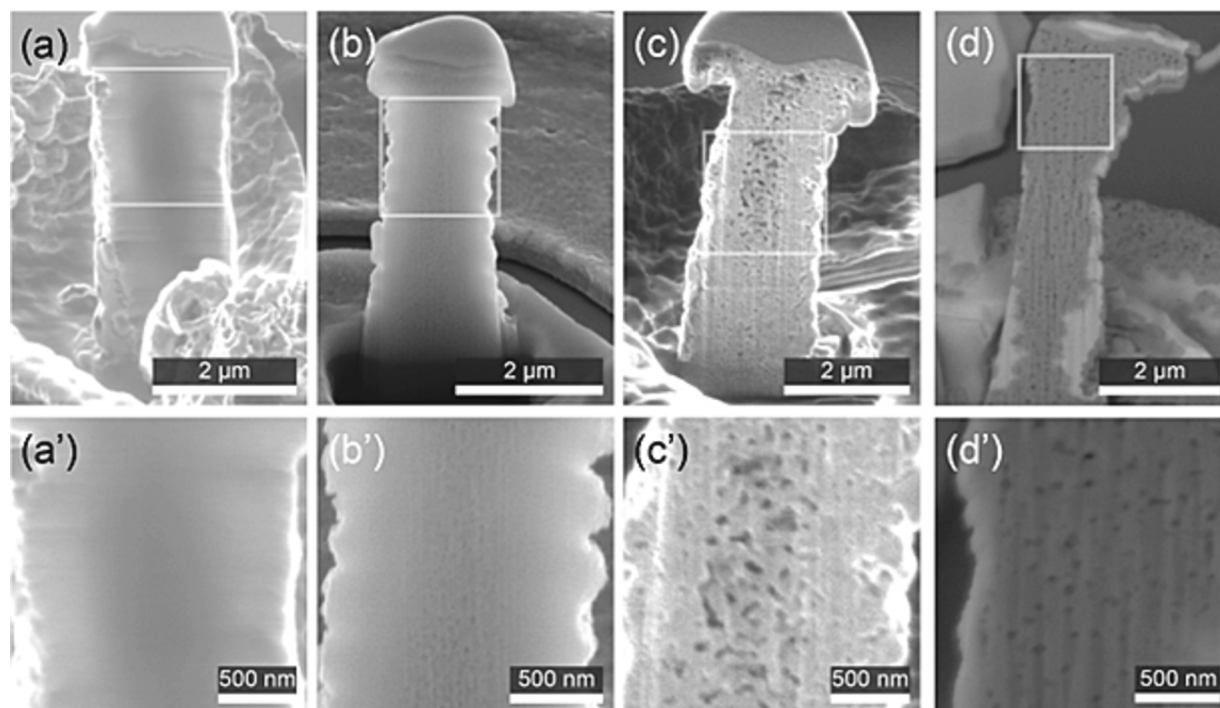


**Fig. 8.** Secondary electron contrast micrographs of FIB-milled cross-sections of 10 mol% YSZ non-compressed micropillars annealed at (a) 600 °C for 1 h, (b) 900 °C for 1 h, (c) 1050 °C for 1 h, (d) 1050 °C for 2 h, and (a' – d') high-magnification images presenting the cores of (a – d) micropillars.

YSZ micropillars are likely affected by factors other than carbon impurities.

The global trend in compression strength (Fig. 9) is most likely associated with the Hall–Petch strengthening, as it inversely correlates with the average crystallite size increase from  $5.2 \pm 0.6$  nm to  $25.2 \pm 1.7$  nm for annealing at 600 °C for 1 h, and at 1050 °C for 2 h,

respectively (Table S2; Fig. S8). [52–54] Furthermore, material imperfections, such as pores, likely cause the overproportional compression strength to decrease, especially when micropillars annealed for 1 h at 900 °C and 1050 °C are compared. The pore volume surge predominantly takes place within the micropillar cores. These pores primarily stem from the combustion of volatile components transforming into a



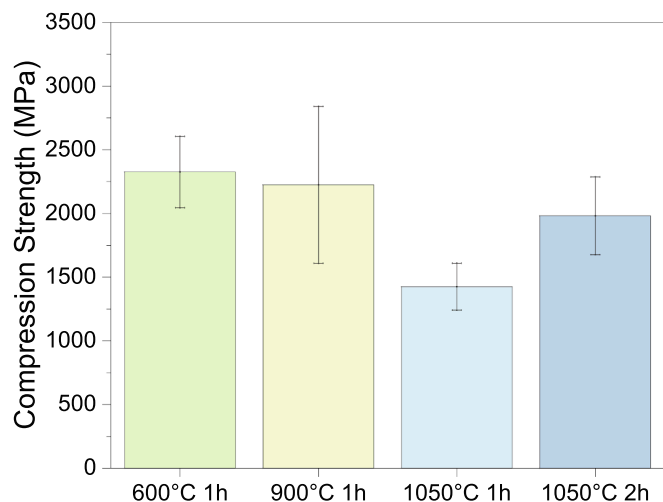


Fig. 9. Compression strength for 10 mol % YSZ micropillars annealed for 1 h at 600 °C, 900 °C, and 1050 °C, and for 2 h at 1050 °C.

gaseous state. We propose that while within the peripheral regions of the pillars, these gas bubbles can disperse towards the exposed surface, they encounter confinement within the core, where they steadily expand due to escalating internal pressure at higher annealing temperatures.

Furthermore, agglomeration of pores can occur and explain the increased pore sizes (Fig. 8a – c). An additional hour of annealing at 1050 °C (1 h vs 2 h) increases compression strength, and the FIB-milled cross-section (Fig. 8d) reveals a homogenous pore distribution. This can be attributed to the migration of pores originating from the interior towards the exterior parts of micropillars, allowed by the longer annealing time, leading to a more uniform pore distribution across the microstructure. Likewise, promoted sintering effects can explain the increased strength and brittleness. Compared to the 2 h treatment at 1050 °C, inferior properties of pillars annealed at 1050 °C for 1 h could also be related to the impurities mentioned above with Zr-O bond distortion and the higher amount of oxygen defects in the micropillar.

Kulyk *et al.* [55] investigated the strength and fracture behavior of Y-stabilized zirconia concerning the  $Y_2O_3$  content (3 to 8 at%) produced by sintering powder precursors. The authors observed that the most favorable fracture mechanism occurs when: (i) the sintering promotes a full recrystallization of the microstructure. In this case, the agglomerates of fine grains with high grain boundary bond strength are the dominant features of the fracture surface, with the crack propagating along the grain boundaries of the grains/agglomerates, and only a few grains are cleaved. An alternative mechanism (ii) is described by supposing pronounced grain growth. However, increased amount of cleaved grains can reduce the strengths. In contrast, (iii) other mechanisms can take place for a less pronounced recrystallization process, which might result in grains having weak cohesion, reducing the grain/agglomerate boundaries' bonding strength.

Concerning the proposed fracture behavior by Kulyk *et al.* [55], we assume that fracture mainly occurs for the "full crystallization" mechanism (i). However, a higher annealing temperature and respectively grain size could lead to more cleaved grains. Nonetheless, this might be a contributing fracture effect in our micropillars; we should recall that the crystallite sizes in this work are 5.2 nm to 29.1 nm (Table S2), and therefore significantly smaller from 0.6 – 1.0 mm studied by Kulyk *et al.* [55] This leads us to exclude other mechanisms, such as crack propagation mainly caused by large cleaved grains mentioned in (ii). Furthermore, as shown in Fig. S2, the starting condition of the samples in this work is a non-crystalline pre-ceramic photopolymer. Therefore, fracture mechanism (iii) is unlikely because it assumes a microstructure with partially sintered particles of the initial crystalline powder mixture.

### 3. Conclusions

The tailor-made photoresin containing monomeric salts of zirconium and yttrium enables the additive manufacturing of yttria-stabilized zirconia arbitrarily shaped microarchitectures with sub-micrometer precision. The monomeric zirconium and yttrium salts are compatible and miscible within the 3D photopolymer microarchitecture formed via TPL. The result is of significant importance for fabricating 3D mixed oxide microarchitectures through TPL and opens a promising avenue for further studies on structurally refined advanced ceramic materials. [56, 57] The applied solvent system permits doping, as previously presented for  $ZrO_2$  microarchitectures hosting different lanthanide species. [46, 47, 56]

The crystallization of YSZ is not directly initiated during the TPL process but triggered by thermal annealing and combustion of organic photopolymer organic constituents. Annealing at a temperature as low as 600 °C yields a crystalline product, with crystallinity further improving with the annealing temperature. The doping of  $ZrO_2$  with  $\approx 10$  mol%  $Y_2O_3$  yields the *c*- $ZrO_2$  phase; a portion of the product is of reduced stoichiometry. The STEM analysis of the sample annealed at 1200 °C for 2 h unveils that the structure comprises grains of average  $121 \pm 21$  nm length and  $89 \pm 15$  nm width, approximately four times larger than the crystallites estimated using the Scherrer equation.

Upon UV excitation, defect-related yellowish-green emission is observed from 10 mol% YSZ 3D microarchitectures, associated with intrinsic (F) and extrinsic ( $F_A$  and  $F_{AA}$ ) centers, correlated with the charge compensation within the anionic and cationic sublattice associated with  $Y^{3+}$  doping. The emissions are stable and comparable between the annealing temperatures. Such stable optical properties could be utilized, e.g., in high-temperature phosphor thermometry, where YSZ is often a material of choice. [46, 58]

The microcompression experiments reveal that the intrinsic mechanical strength of YSZ micropillars is the highest for micropillars annealed at 600 °C and decreases with increasing annealing temperature. At the same time, their deformation behavior changes from ductile to brittle-like. The Hall–Petch strengthening mechanism and increasing porosity most likely explain the findings. The 10 mol% YSZ micropillars annealed for 1 h at 600 °C fail at  $2.3 \pm 0.3$  GPa and perform similarly to *m*- $ZrO_2$  micropillars presented in our previous study [51], while the mechanical stability of 10 mol% YSZ micropillars annealed at 1050 °C for 1 h resembles *t*- $ZrO_2$ . Further composition tuning and incorporating carbon-based remnants to yield a "brick and mortar" composite with YSZ could be an interesting path for future studies.

### 4. Experimental procedure

**Materials:** Acrylic acid (CAS: 79–10-7, stabilized with ca 200 ppm 4-methoxyphenol, 99 %), dichloromethane (CAS: 75–09-2, 99.9 %), and dimethyl sulfoxide (CAS: 67–68-5, 99+%) were supplied by Alfa Aesar. Dimethylacetamide (CAS: 127–19-5, anhydrous, 99.8 %), dimethylsulfoxide (CAS: 67–68-5, ACS reagent,  $\geq 99.9$  %), methanol (CAS: 67–56-1, anhydrous, 99.8 %), pentaerythritol triacrylate (CAS: 3524–68-3), and zirconium acrylate (CAS: 60653–57-8) were purchased from Sigma Aldrich. Yttrium methacrylate (CAS: 79718–33-5) and 7-Diethylamino-3-thenoylcoumarin (CAS: 77820–11-2, 97 %) were delivered by Gelest and J&K Scientific. Agents were used as received without additional purification.

#### 4.1. Tailor-made organic-inorganic resins for two-photon lithography

Custom resin allowing the additive manufacturing of 10 mol%  $Y_2O_3$  stabilized  $ZrO_2$  ( $\approx 17.0$  wt%  $Y_2O_3$ ) was prepared using zirconium acrylate (65.05 mg) and yttrium methacrylate hydrate (13.3 mg). The salts were placed in an amber round bottom flask, into which acrylic acid (150 mg), dimethylacetamide (500 mg), and dichloromethane (2.0 g) were poured. The contents were agitated using a rotary evaporator



operated at ambient pressure at 40 °C for 45 min until the complete dissolution of salts. To the flask, pentaerythritol triacrylate (300 mg) was added, and the contents were mixed for 30 min, after which 7-diethylamino-3-thenoylcoumarin (23 mg) and dichloromethane (100 mg) were added. The mixing continued for 15 min, after which the pressure was reduced for 45 min to evaporate dichloromethane. The freshly prepared resin was used directly. In the modified recipe applied to yield 4.2 mol%  $Y_2O_3$  ( $\approx 7.4$  wt%  $Y_2O_3$ ), the amount of zirconium acrylate and yttrium methacrylate hydrate were adjusted to 72.5 mg and 5.8 mg, respectively, maintaining the total amount of salts at approximately 210  $\mu$ mol. The  $Y_2O_3$  reference powder is yielded by modification of the original recipe, and 72.3 mg of yttrium methacrylate hydrate is used without zirconium acrylate.

#### 4.2. Two-photon lithography

Pre-ceramic microstructures composed of metal-containing polymers were manufactured with a commercial two-photon lithography system (Photonic GT, Nanoscribe GmbH). On the top side of the glass cover slide ( $\varnothing 30$  mm) mounted into a holder, Two Kapton® double-side tape strips were attached, between which a droplet of resin was pipetted and covered with a Si chip (1 x 1 cm). A spot of immersion oil (Immersionol™ 518F, Carl Zeiss) was applied on the opposite side. The system was equipped with a 63x/1.4NA oil immersion objective (Plan-Apochromat, Carl Zeiss), and the interface between Si and resin was first manually set in a reflection mode. A scanning speed of 1 mm s<sup>-1</sup> and 18.9 mW laser power was applied during printing, and the stitching and hatching distance of 0.4  $\mu$ m were applied. After successful structuring, substrates with printed 3D pre-ceramic architectures were dipped in DMSO for 5 min and in methanol for 2 min to remove the non-polymerized resin. The prepared samples were then placed in an oven at 65 °C to dry and provide additional curing.

#### 4.3. Synthesis of reference powders

The tailor-made resin was cast on a Petri dish and cured for 4 h with a 365 nm UV lamp (36 W, name). The polymerized material was dried for 1 h in an oven set at 65 °C. The portions of the as-obtained cured pre-ceramic material were then annealed in the air to synthesize the control powders.

#### 4.4. Thermal treatment

The 3D-printed samples and portions of UV-cured resin were thermally treated in the air to combust the organic constituents and facilitate the crystallization of the target ceramic products. The samples were placed in Alsint® crucibles and annealed in a chamber oven (LH 15/12, Nabertherm) with opened air inlets. The two-stage annealing included a slow heating ramp step (0.4 min<sup>-1</sup>) to reach 350 °C, followed by a faster ramp (1° min<sup>-1</sup>) to the target temperature (600 °C, 750 °C, 900 °C, 1050 °C and 1200 °C, respectively). The samples were annealed for 1 h or 2 h and then cooled to room temperature at a natural rate.

#### 4.5. Characterization

##### 4.5.1. Morphology and mechanical properties

**Scanning Electron Microscopy (SEM):** The high-magnification topographical mapping of the samples was conducted using an HR-SEM system (Zeiss Merlin) with a high-efficiency secondary electron detector (HE-SE2) and 1.3 kV acceleration voltage.

**Pillar compression:** The compression experiments were conducted with a Femtotools NMT03 nanomechanical testing system installed within a Zeiss Cross Beam 1540EsB FIB workstation. The deformation of pillars was continuously observed until the fracture using a displacement-controlled mode at 20 nm s<sup>-1</sup> testing speed.

##### 4.5.2. Chemical composition and material characterization

**X-Ray Powder Diffraction (XRD):** The crystalline structure of the reference powders was characterized by an X-ray powder diffractometer (D2 Phaser, Bruker), using Cu-K $\alpha$  source radiation ( $\lambda = 1.5418$  Å) operated at 10 mA and 30 kV, and a LynxEye detector. The scan within the 20 – 80° 2 $\theta$  scan range was conducted with 0.02° step and 2.25° min<sup>-1</sup> scan speed. The samples were cast on a zero-diffraction Si sample holder (Bruker). The baseline correction was done with CrystalSleuth software.

**Confocal Raman Spectroscopy (Raman):** Room-temperature Raman spectroscopy measurements of the 3D-printed structures and reference powders were conducted using a Confocal Raman Microscope (Alpha 300, WiTec) equipped with a 600 g/mm grating and 100x/0.9A (MPlan FL N, Olympus) air objective. The materials were excited with a 532 nm (frequency-doubled Nd:YAG) laser operated at 10 mW and characterized in a standard backscattered mode. For each sample, ten 25 s acquisitions were averaged. The baseline correction and cosmic-ray removal were done using CrystalSleuth software. Powder samples were placed on Raman-grade CaF<sub>2</sub> substrates (Knight Optical) and dispersed evenly with drop-cast isopropanol.

**Energy Dispersive X-ray Spectroscopy (EDX):** The elemental distribution was assessed by EDX attachment (name) to the SEM (name), using AZtec (Oxford Scientific) software for acquisition.

**Thermogravimetric analysis (TGA):** The UV-cured dried resin was transferred to a platinum crucible and heated in the air at a 5 °C min<sup>-1</sup> rate from 37 °C to 1200 °C using a thermal analyzer (STA 449 F3, Netzsch).

**X-ray Photoelectron Spectroscopy (XPS):** The control powder samples annealed at 600 °C, 900 °C, and 1050 °C for 1 h, and 1050 °C for 2 h were characterized. The analysis was performed with a PHI Quantescan XPS/HAXPES microprobe with a monochromatic source of 1486.6 eV (Al K $\alpha$ ) radiation (25 W, 15 kV). The general survey spectra were collected using 280 eV pass energy at 1 eV step size, while the core regions were analyzed using 112 eV pass energy at 0.1 eV step size. The Tougaard and Shirley background types were used, and the synthetic Voigt peaks were fitted using CasaXPS software. All spectra were calibrated to the 284.8 eV aliphatic carbon signal. The 2.4 eV and 2.05 eV splitting were fixed for the Zr 3d<sub>5/2</sub>/Zr 3d<sub>3/2</sub> and Y 3d<sub>5/2</sub>/Y 3d<sub>3/2</sub> peaks, respectively. The 3:2 ratios of 3d<sub>5/2</sub> and 3d<sub>3/2</sub> peak areas are maintained.

**Focused Ion Beam (FIB):** The cross-section lamellae were extracted from the 3D-printed microarchitectures using a Helios 5 UX DualBeam (Thermo Scientific™) workstation. The initial milling was performed using a Ga source, thinning, and polishing with low-energy W and Si ions. The lamellae were welded to a Cu grid using W and C and analyzed with STEM.

The micropillar cross-sections were milled with Ga<sup>+</sup> in an FEI Versa3D Dual Beam station. Partial Pt coating was used to prevent curtaining and protect the pillars from damage.

**Scanning Transmission Electron Microscopy (STEM):** Scanning Transmission Electron Microscopy (STEM) analysis of lamellas prepared by FIB was conducted using a Spectra 300 station (Thermo Scientific™) operated at 300 kV acceleration voltage and 173 pA current.

**Photoluminescence ( $\mu$ -PL):** The micro-photoluminescence spectra were registered at room temperature with a Horiba Jobin-Yvon LabRAM Hr800 confocal microscope setup using a 40x/0.47NA MicroSpot® Focusing Objective (LMU-40X-NUV, Thorlabs), and a 325 nm excitation source (He-Cd IK Series, Kimmon Koha). Each spectrum is an average of ten accumulations of 1 s, registered with a 600 l/mm grating and a D 3 filter.

#### Author contributions

J. P. W.: conceptualization, methodology, validation, formal analysis, investigation, data curation, writing – original draft, writing – review & editing, visualization, supervision, project administration; S. Z.: methodology, validation, formal analysis, investigation, data curation,

writing – original draft, writing – review & editing, visualization, project administration; S.G. methodology, validation, formal analysis, investigation, data curation, writing – review & editing, project administration; D. M.: resources, writing – review & editing, resources, supervision, B.M. and J. G. E. G.: conceptualization, validation, resources, writing – review & editing, supervision, project administration, funding acquisition; A. S. A.: conceptualization, methodology, writing – original draft, writing – review & editing, supervision, project administration.

### Declaration of competing interest

The authors declare that they have no known competing financial interests or personal relationships that could have appeared to influence the work reported in this paper.

### Data availability

Data will be made available on request.

### Acknowledgments

The authors express gratitude to Mark Smithers and Gerhard Hawranek for acquiring high-resolution SEM images, Dr. Yibin Bu for collecting the XPS spectra, and Cindy Huiskes for performing the TGA. The authors thank Dr. Melissa Goodwin, Dr. Christina Kainz, and Hendrik Holz for their assistance during the FIB milling. The authors thank Dr. Martina Tsvetanova and Dr. Rico Kein for their help with the STEM analysis.

The samples were manufactured at the MESA + Institute for Nanotechnology. The materials were analyzed at the MESA + Institute for Nanotechnology and Live Cell Imaging Facility of the University of Twente. The mechanical properties were characterized at the Department of Materials Science and Engineering at Friedrich-Alexander-Universität Erlangen-Nürnberg.

The research of J.P.W, A.S.A., and H.G was funded by the European Research Council (ERC) under the Horizon 2020 research and innovation programme of the European Union (Grant Agreement 742004). The contribution of S.Z., S.G., and B.M. to this project has received funding from the European Research Council (ERC) under the European Union's Horizon 2020 research and innovation programme (Grant Agreement 949626). D.M. acknowledges financial support from MICINN (PID2021-122562NB-I00).

### Appendix A. Supplementary data

Supplementary data to this article can be found online at <https://doi.org/10.1016/j.matdes.2024.112701>.

### References

- R. H. Nielsen, J. H. Schlewitz, H. Nielsen, Updated by Staff, Zirconium and Zirconium Compounds, in: Kirk-Othmer Encycl. Chem. Technol., John Wiley & Sons, Inc., Hoboken, NJ, USA, 2007: pp. 621–664. <https://doi.org/10.1002/0471238961.26091803.a01.pub2>.
- J. Arriaga Dávila, J.P. Winczewski, M. Herrera-Zaldívar, E.A. Murillo-Bracamontes, C. Rosero Arias, N. Pineda-Aguilar, J.L. Cholula-Díaz, I. De Leon, H. Gardeniers, A. Susarrey Arce, E. Martínez-Guerra, Enabling high-quality transparent conductive oxide on 3D printed ZrO<sub>2</sub> architectures through atomic layer deposition, *Appl. Surf. Sci.* 636 (2023) 157796, <https://doi.org/10.1016/j.apsusc.2023.157796>.
- J. Robert Kelly, I. Denry, Stabilized zirconia as a structural ceramic: An overview☆, *Dent. Mater.* 24 (2008) 289–298, <https://doi.org/10.1016/j.dental.2007.05.005>.
- A. Navrotsky, Thermochemical insights into refractory ceramic materials based on oxides with large tetravalent cations, *J. Mater. Chem.* 15 (2005) 1883, <https://doi.org/10.1039/b417143h>.
- S. Fabris, A stabilization mechanism of zirconia based on oxygen vacancies only, *Acta Mater.* 50 (2002) 5171–5178, [https://doi.org/10.1016/S1359-6454\(02\)00385-3](https://doi.org/10.1016/S1359-6454(02)00385-3).
- J.D. Ballard, J. Davenport, C. Lewis, W. Nelson, R.H. Doremus, L.S. Schadler, Phase Stability of Thermal Barrier Coatings Made From 8 wt.% Yttria Stabilized Zirconia: A Technical Note, *J. Therm. Spray Technol.* 12 (2003) 34–37, <https://doi.org/10.1361/105996303770348474>.
- Q. Liu, S. Huang, A. He, Composite ceramics thermal barrier coatings of yttria stabilized zirconia for aero-engines, *J. Mater. Sci. Technol.* 35 (2019) 2814–2823, <https://doi.org/10.1016/j.jmst.2019.08.003>.
- S.-J. Hao, C. Wang, T.-L. Liu, Z.-M. Mao, Z.-Q. Mao, J.-L. Wang, Fabrication of nanoscale yttria stabilized zirconia for solid oxide fuel cell, *Int. J. Hydrogen Energy.* 42 (2017) 29949–29959, <https://doi.org/10.1016/j.ijhydene.2017.08.143>.
- M. Kaplan, J. Park, S. Young Kim, A. Ozturk, Production and properties of tooth-colored yttria stabilized zirconia ceramics for dental applications, *Ceram. Int.* 44 (2018) 2413–2418, <https://doi.org/10.1016/j.ceramint.2017.10.211>.
- A.-M. Azad, Fabrication of yttria-stabilized zirconia nanofibers by electrospinning, *Mater. Lett.* 60 (2006) 67–72, <https://doi.org/10.1016/j.matlet.2005.07.085>.
- V.V. Rodaev, S.S. Razlivalova, A.O. Zhigachev, V.M. Vasyukov, Y.I. Golovin, Preparation of Zirconia Nanofibers by Electrospinning and Calcination with Zirconium Acetylacetonate as Precursor, *Polymers (basel)*. 11 (2019) 1067, <https://doi.org/10.3390/polym11061067>.
- C.C. Wei, K. Li, Yttria-stabilized zirconia (YSZ)-based hollow fiber solid oxide fuel cells, *Ind. Eng. Chem. Res.* 47 (2008) 1506–1512, <https://doi.org/10.1021/ie070960v>.
- T. Tätté, M. Part, R. Talviste, K. Hanschmidt, K. Utt, U. Mäeorg, I. Jögi, V. Kiisk, H. Mändar, G. Nurk, P. Rauwel, Yttria stabilized zirconia microtubes for microfluidics under extreme conditions, *RSC Adv.* 4 (2014) 17413–17419, <https://doi.org/10.1039/C4RA00621F>.
- L. Ferrage, G. Bertrand, P. Lenormand, Dense yttria-stabilized zirconia obtained by direct selective laser sintering, *Addit. Manuf.* 21 (2018) 472–478, <https://doi.org/10.1016/j.addma.2018.02.005>.
- I. Buj-Corral, D. Vidal, A. Tejo-Otero, J.A. Padilla, E. Xuriguera, F. Fenollosa-Artés, Characterization of 3D Printed Yttria-Stabilized Zirconia Parts for Use in Prostheses, *Nanomaterials*. 11 (2021) 2942, <https://doi.org/10.3390/nano11112942>.
- A. Pesce, A. Hornés, M. Núñez, A. Morata, M. Torrell, A. Tarancón, 3D printing the next generation of enhanced solid oxide fuel and electrolysis cells, *J. Mater. Chem. A.* 8 (2020) 16926–16932, <https://doi.org/10.1039/D0TA02803G>.
- J. Zhang, L. Wei, X. Meng, F. Yu, N. Yang, S. Liu, Digital light processing-stereolithography three-dimensional printing of yttria-stabilized zirconia, *Ceram. Int.* 46 (2020) 8745–8753, <https://doi.org/10.1016/j.ceramint.2019.12.113>.
- L. Wei, J. Zhang, F. Yu, W. Zhang, X. Meng, N. Yang, S. Liu, A novel fabrication of yttria-stabilized-zirconia dense electrolyte for solid oxide fuel cells by 3D printing technique, *Int. J. Hydrogen Energy.* 44 (2019) 6182–6191, <https://doi.org/10.1016/j.ijhydene.2019.01.071>.
- A. Desponds, A. Banyasz, D. Chateau, A. Tellal, A. Venier, S. Meille, G. Montagnac, J. Chevalier, C. Andraud, P.L. Baldeck, S. Parola, 3D Printing and Pyrolysis and Optical ZrO<sub>2</sub> Nanostructures by Two-Photon Lithography: Reduced Shrinkage and Crystallization Mediated by Nanoparticles Seeds, *Small*. 17 (2021) 2102486, <https://doi.org/10.1002/sml.202102486>.
- S.S. Rodaev, V.V. Razlivalova, A.I. Tyurin, A.O. Zhigachev, Y.I. Golovin, Microstructure and Phase Composition of Yttria-Stabilized Zirconia Nanofibers Prepared by High-Temperature Calcination of Electrospun Zirconium Acetylacetonate/Yttrium Nitrate/Polyacrylonitrile Fibers, *Fibers*. 7 (2019), <https://doi.org/10.3390/fib710008>.
- F.G.R. Gimblett, A. Hussain, K.S.W. Sing, Thermal and related studies of some basic zirconium salts, *J. Therm. Anal.* 34 (1988) 1001–1013, <https://doi.org/10.1007/BF01913505>.
- S.N. Basahel, T.T. Ali, M. Mokhtar, K. Narasimharao, Influence of crystal structure of nanosized ZrO<sub>2</sub> on photocatalytic degradation of methyl orange, *Nanoscale Res. Lett.* 10 (2015) 73, <https://doi.org/10.1186/s11671-015-0780-z>.
- J.B. Kortright, A.C. Thompson, X-Ray Emission Energies, in: A.C. Thompson (Ed.), X-Ray Data Book, 3rd ed., Lawrence Berkeley National Laboratory, University of California, Berkeley, CA, USA, 2009: pp. 8–27.
- A. Feinberg, C.H. Perry, Structural disorder and phase transitions in ZrO<sub>2</sub>-Y<sub>2</sub>O<sub>3</sub> system, *J. Phys. Chem. Solids.* 42 (1981) 513–518, [https://doi.org/10.1016/0022-3697\(81\)90032-9](https://doi.org/10.1016/0022-3697(81)90032-9).
- C.N. Chervin, B.J. Clapsaddle, H.W. Chiu, A.E. Gash, J.H. Satcher, S.M. Kaulzarich, Aerogel Synthesis of Yttria-Stabilized Zirconia by a Non-Alkoxide Sol–Gel Route, *Chem. Mater.* 17 (2005) 3345–3351, <https://doi.org/10.1021/cm0503679>.
- C.G. Kontoyannis, M. Orkoulia, Quantitative determination of the cubic, tetragonal and monoclinic phases in partially stabilized zirconias by Raman spectroscopy, *J. Mater. Sci.* 29 (1994) 5316–5320, <https://doi.org/10.1007/BF01171541>.
- Y. Hemberger, N. Wichtner, C. Berthold, K.G. Nickel, Quantification of Yttria in Stabilized Zirconia by Raman Spectroscopy, *Int. J. Appl. Ceram. Technol.* 13 (2016) 116–124, <https://doi.org/10.1111/ijac.12434>.
- M.B. Pomfret, C. Stoltz, B. Varughese, R.A. Walker, Structural and Compositional Characterization of Yttria-Stabilized Zirconia: Evidence of Surface-Stabilized, Low-Valence Metal Species, *Anal. Chem.* 77 (2005) 1791–1795, <https://doi.org/10.1021/ac048600u>.
- S. Ghosh, D. Teweldebrhan, J.R. Morales, J.E. Garay, A.A. Balandin, Thermal properties of the optically transparent pore-free nanostructured yttria-stabilized zirconia, *J. Appl. Phys.* 106 (2009) 113507, <https://doi.org/10.1063/1.3264613>.
- W. Zhu, S. Nakashima, E. Marin, H. Gu, G. Pezzotti, Microscopic mapping of dopant content and its link to the structural and thermal stability of yttria-stabilized zirconia polycrystals, *J. Mater. Sci.* 55 (2020) 524–534, <https://doi.org/10.1007/s10853-019-04080-9>.

- [31] P.G. Spizzirri, J.H. Fang, S. Rubanov, E. Gauja, S. Prawer, Nano-Raman spectroscopy of silicon surfaces, *Mater. Forum.* 34 (2010) 161–166, <https://doi.org/10.48550/arXiv.1002.2692>.
- [32] Q. Wen, Z. Yu, R. Riedel, The fate and role of in situ formed carbon in polymer-derived ceramics, *Prog. Mater. Sci.* 109 (2020) 100623, <https://doi.org/10.1016/j.pmatsci.2019.100623>.
- [33] A. Zakhurdaeva, P.I. Dietrich, H. Hölscher, C. Koos, J.G. Korvink, S. Sharma, Custom-designed glassy carbon tips for atomic force microscopy, *Micromachines.* 8 (2017) 1–10, <https://doi.org/10.3390/mi8090285>.
- [34] S.K. Jerng, D.S. Yu, J.H. Lee, C. Kim, S. Yoon, S.H. Chun, Graphitic carbon growth on crystalline and amorphous oxide substrates using molecular beam epitaxy, *Nanoscale Res. Lett.* 6 (2011) 1–6, <https://doi.org/10.1186/1556-276X-6-565>.
- [35] S.A. Cotton, Titanium, zirconium and hafnium, *Annu. Reports Prog. Chem. – Sect. A.* 93 (1997) 143–153, <https://doi.org/10.1039/ic9969300143>.
- [36] A.M. Huerta-Flores, F. Ruiz-Zepeda, C. Eyovge, J.P. Winczewski, M. Vandichel, M. Gabersček, N.D. Boscher, H.J.G.E. Gardeniers, L.M. Torres-Martínez, A. Susarrey-Arce, Enhanced Photocatalytic Hydrogen Evolution from Water Splitting on Ta<sub>2</sub>O<sub>5</sub>/SrZrO<sub>3</sub> Heterostructures Decorated with Cu<sub>x</sub>O/RuO<sub>2</sub> Cocatalysts, *ACS Appl. Mater. Interfaces.* 14 (2022) 31767–31781, <https://doi.org/10.1021/acsmi.2c02520>.
- [37] P. Gruene, D.M. Rayner, B. Redlich, A.F.G. van der Meer, J.T. Lyon, G. Meijer, A. Fielićke, Colossal Ionic Conductivity at Interfaces of Epitaxial ZrO<sub>2</sub>:Y<sub>2</sub>O<sub>3</sub>/SrTiO<sub>3</sub> Heterostructures, *Science (80-.)*. 321 (2008) 674–676, <https://doi.org/10.1126/science.1161166>.
- [38] Z. Cheng, H. Ren, Y. Wang, S. Ta, P. Zhang, Y. Yang, S. Xu, B.A. Goodman, W. Deng, Effects of Yb<sub>2</sub>O<sub>3</sub> as Stabilizer and Sensitizer on the Luminescence Properties of Cubic ZrO<sub>2</sub> Single Crystals, *Cryst. Growth Des.* 22 (2022) 5481–5488, <https://doi.org/10.1021/acs.cgd.2c00562>.
- [39] N.V. Vlasenko, P.I. Kyriienko, K.V. Valihura, G.R. Kosmambetova, S.O. Soloviev, P. E. Strizhak, Yttria-Stabilized Zirconia as a High-Performance Catalyst for Ethanol to n-Butanol Guerbet Coupling, *ACS Omega.* 4 (2019) 21469–21476, <https://doi.org/10.1021/acsomega.9b03170>.
- [40] N.G. Petrik, D.P. Taylor, T.M. Orlando, Laser-stimulated luminescence of yttria-stabilized cubic zirconia crystals, *J. Appl. Phys.* 85 (1999) 6770–6776, <https://doi.org/10.1063/1.370192>.
- [41] I.J. Berlin, V.S. Anitha, P.V. Thomas, K. Joy, Influence of oxygen atmosphere on the photoluminescence properties of sol-gel derived ZrO<sub>2</sub> thin films, *J. Sol-Gel Sci. Technol.* 64 (2012) 289–296, <https://doi.org/10.1007/s10971-012-2856-x>.
- [42] Z. Wang, B. Yang, Z. Fu, W. Dong, Y. Yang, W. Liu, UV-blue photoluminescence from ZrO<sub>2</sub> nanopowders prepared via glycine nitrate process, *Appl. Phys. A Mater. Sci. Process.* 81 (2005) 691–694, <https://doi.org/10.1007/s00339-005-3238-9>.
- [43] C. Zhang, C. Li, J. Yang, Z. Cheng, Z. Hou, Y. Fan, J. Lin, Tunable luminescence in monodisperse zirconia spheres, *Langmuir.* 25 (2009) 7078–7083, <https://doi.org/10.1021/la900146y>.
- [44] M. Boffelli, W. Zhu, M. Back, G. Sponchia, T. Francese, P. Riello, A. Benedetti, G. Pezzotti, Oxygen Hole States in Zirconia Lattices: Quantitative Aspects of Their Cathodoluminescence Emission, *J. Phys. Chem. A.* 118 (2014) 9828–9836, <https://doi.org/10.1021/jp506923p>.
- [45] J.-M. Costantini, Y. Watanabe, K. Yasuda, M. Fasoli, Cathodo-luminescence of color centers induced in sapphire and yttria-stabilized zirconia by high-energy electrons, *J. Appl. Phys.* 121 (2017) 153101, <https://doi.org/10.1063/1.4980111>.
- [46] J. Winczewski, M. Herrera, C. Cabriel, I. Izeddin, S. Gabel, B. Merle, A. Susarrey Arce, H. Gardeniers, Additive Manufacturing of 3D Luminescent ZrO<sub>2</sub>:Eu<sup>3+</sup> Architectures, *Adv. Opt. Mater.* 10 (2022) 2102758, <https://doi.org/10.1002/adom.202102758>.
- [47] J. Winczewski, M. Herrera, H. Gardeniers, A. Susarrey-Arce, White emission in 3D-printed phosphor microstructures, *Chem. Commun.* 59 (2023) 3095–3098, <https://doi.org/10.1039/D2CC06953A>.
- [48] K. Smits, L. Grigorjeva, D. Millers, A. Sarakovskis, J. Grabis, W. Lojkowski, Intrinsic defect related luminescence in ZrO<sub>2</sub>, *J. Lumin.* 131 (2011) 2058–2062, <https://doi.org/10.1016/j.jlumin.2011.05.018>.
- [49] W. Zhu, S. Nakashima, E. Marin, H. Gu, G. Pezzotti, Annealing-Induced Off-Stoichiometric and Structural Alterations in Ca<sup>2+</sup>- and Y<sup>3+</sup>-Stabilized Zirconia Ceramics, *Materials (basel).* 14 (2021) 5555, <https://doi.org/10.3390/ma14195555>.
- [50] K. Hachiya, H. Oku, J. Kondoh, Photoluminescence in yttria-stabilized zirconia of aging effects, *Phys. Rev. B.* 71 (2005) 064111, <https://doi.org/10.1103/PhysRevB.71.064111>.
- [51] J.P. Winczewski, S. Zeiler, S. Gabel, A. Susarrey-Arce, J.G.E. Gardeniers, B. Merle, Exploring the mechanical properties of additively manufactured carbon-rich zirconia 3D microarchitectures, *Mater. Des.* 232 (2023) 112142, <https://doi.org/10.1016/j.matdes.2023.112142>.
- [52] E.O. Hall, The Deformation and Ageing of Mild Steel: III Discussion of Results, *Proc. Phys. Soc. Sect. B.* 64 (1951) 747–753, <https://doi.org/10.1088/0370-1301/64/9/303>.
- [53] N.J. Petch, The Cleavage Strength of Polycrystals, *J. Iron Steel Inst.* 174 (1953) 25–28.
- [54] C.S. Pande, K.P. Cooper, Nanomechanics of Hall-Petch relationship in nanocrystalline materials, *Prog. Mater. Sci.* 54 (2009) 689–706, <https://doi.org/10.1016/j.pmatsci.2009.03.008>.
- [55] V. Kulyk, Z. Duriagina, A. Kostryzhev, B. Vasylyv, V. Vavruk, O. Marenych, The Effect of Yttria Content on Microstructure, Strength, and Fracture Behavior of Yttria-Stabilized Zirconia, *Materials (basel).* 15 (2022) 5212, <https://doi.org/10.3390/ma15155212>.
- [56] J. Winczewski, J. Arriaga-Dávila, C. Rosero-Arias, A. Susarrey-Arce, Tailoring chemistry for inorganic 3D micro-optics, *Trends Chem.* (2024), <https://doi.org/10.1016/j.trechm.2023.12.005>.
- [57] J.P. Winczewski, J. Arriaga Dávila, M. Herrera-Zaldívar, F. Ruiz-Zepeda, R.M. Córdova-Castro, C.R. Pérez de la Vega, C. Cabriel, I. Izeddin, H. Gardeniers, A. Susarrey-Arce, 3D-Architected Alkaline-Earth Perovskites, *Adv. Mater.* (2024) 2307077, <https://doi.org/10.1002/adma.202307077>.
- [58] J.P. Feist, A.L. Heyes, Europium-doped yttria-stabilized zirconia for high-temperature phosphor thermometry, *Proc. Inst. Mech. Eng. Part L J. Mater. Des. Appl.* 214 (2000) 7–12, <https://doi.org/10.1177/146442070021400102>.